In situ measurements of twist and bend elastic constants in the oblique helicoidal cholesteric

Olena S. Iadlovska, 1,2 Kamal Thapa, 1,2 Mojtaba Rajabi, 1,2 Sergij V. Shiyanovskii, 1,3 and Oleg D. Lavrentovich ¹Advanced Materials and Liquid Crystal Institute, Kent State University, Kent, Ohio 44242, USA ²Department of Physics, Kent State University, Kent, Ohio 44242, USA ³Materials Science Graduate Program, Kent State University, Kent, Ohio 44242, USA

(Received 29 March 2022; accepted 4 May 2022; published 4 August 2022)

Unique electro-optical properties of the oblique helicoidal cholesteric (Ch_{OH}) stem from its heliconical director structure. An applied electric field preserves the single-harmonic modulation of the director while tuning the ChOH period and the corresponding Bragg-peak wavelength within a broad spectral range. We use the response of Ch_{OH} to the electric field to measure the elastic constants of twist K₂₂ and bend K₃₃ directly in the cholesteric phase. The temperature dependencies of K_{22} and K_{33} allow us to determine the range of the electric tunability of the ChOH pitch and the heliconical angle. The data are important for understanding how molecular composition and chirality influence macroscopic elastic properties of the chiral liquid crystals and for the development of Ch_{OH}-based optical devices.

DOI: 10.1103/PhysRevE.106.024702

I. INTRODUCTION

Elastic properties of liquid crystals are determined from the materials' response to external forces such as mechanical stress, and electric and magnetic fields [1,2]. In the nematic (N) liquid crystal, the elastic constants are typically measured by using a uniformly aligned material and applying an electric or magnetic field to create deformations of splay, twist, or bend [3,4]. Application of the same methods to the chiral analog of N, called a cholesteric (Ch), is difficult since the ground state is not uniform: the director twists in space, being perpendicular to the helicoidal axis. A notable exception is the measurement of the Ch twist elastic constant K_{22} by a complete unwinding of the helicoidal structure by an electric or magnetic field [5]. It is often assumed that the elastic constants of Ch have the same values as the ones measured in the N analogs. Such an approximation worsens when chiral molecular interactions become stronger.

Recent research [6] demonstrated that the bend elastic constant K_{33} of Ch could be determined in situ if the material forms the so-called oblique helicoidal cholesteric (Ch_{OH}) structure when exposed to external electromagnetic fields [6–12]. In Ch_{OH}, the director twists around a single axis that is parallel to the applied field, but unlike in a conventional Ch, it is also tilted with respect to the helicoidal axis (Fig. 1). The structure contains both twist and bend of the director. The Ch_{OH} state, predicted theoretically [7,8] and confirmed experimentally [9–11], forms in materials with a low K_{33} , such

Published by the American Physical Society under the terms of the Creative Commons Attribution 4.0 International license. Further distribution of this work must maintain attribution to the author(s) and the published article's title, journal citation, and DOI.

as dimers with flexible aliphatic spacers [13–17]. The period Pand the conical tilt angle θ of the Ch_{OH} structure are defined by the strength of the field and by the material parameters such as dielectric anisotropy, intrinsic pitch, and two elastic constants, K_{22} and K_{33} .

In this work, we demonstrate that the unique structure of Ch_{OH} allows one to measure both K_{22} and K_{33} and their temperature dependencies in the Ch material. The measurement of K_{33} requires one to determine the dielectric anisotropy, refractive indices, and the dependence of the Bragg reflection wavelength on the applied electric field under the normal incidence of light. The K_{22} measurements are more involved and require one to determine the intrinsic (field-free) pitch P_0 , the critical electric field E_{NC} , at which Ch_{OH} unwinds into a uniform structure, and K_{33} . E_{NC} is determined by two different approaches, based on capacitance and interference measurements, which allow one to detect a very small ChOH pitch (below 50 nm) at the fields approaching E_{NC} . These E_{NC} measurement techniques are advantageous as compared to the Bragg reflection or microscopy observations of textures, which are adapted to much larger values of the pitch [9]. Once the moduli K_{22} and K_{33} are measured, other properties could be deduced, such as the range of field tunability of the Ch_{OH} pitch P and the conical angle θ . The proposed protocol thus yields all the static material properties of Ch_{OH}, except for the splay elastic constant.

II. MATERIALS AND EXPERIMENT TECHNIQUES

A. N and Ch materials

A room-temperature N mixture is formulated using flexible dimers 1", 7"-bis(4-cyanobiphenyl-4'-yl) heptane (CB7CB) and 1-(4-cyanobiphenyl-4'-yloxy)-6-(4-cyanobiphenyl-4'-yl) hexane (CB6OCB) (both purchased from SYNTHON Chemicals GmbH & Co. KG), and a rodlike mesogen pentyl

^{*}olavrent@kent.edu

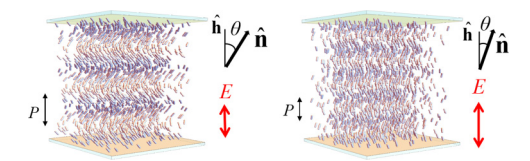


FIG. 1. The oblique helicoidal cholesteric structure Ch_{OH} in an applied electric field: the Ch_{OH} pitch P and the conical angle θ both decrease when the electric field E increases.

cyanobiphenyl (5CB) (EM Industries), in the weight proportion 5CB : CB7CB : CB6OCB = 52 : 31 : 17. The dimer molecules show bend conformations which yield a small K_{33} [13–17], while 5CB shifts the temperature range of the mesophase down to room temperature. The N mixture is doped with the left-handed chiral agent S811 (EM Industries), 5CB : CB7CB : CB6OCB : S811 = 50 : 30 : 16 : 4, to produce the Ch mixture. The mixture without the chiral dopant shows the phase diagram $N_{\rm TB}$ (17.4 °C) N (78 °C) Iso, which is noticeably different from the phase diagram of the Ch mixture: N_{TB}^* (15.5 °C) Ch (66.3 °C) Iso. Here, N_{TB} is the socalled twist-bend nematic phase and N_{TB}^* is its chiral analog; Iso stands for the isotropic phase. The difference suggests that the material properties of the Ch with chiral additive are not the same as those of the achiral N base. The phase diagrams are measured on cooling using Linkam hot stage equipped with the PE94 temperature controller (both Linkam Scientific) and EHEIM Professional-3 cooling system (EHEIM GmbH & Co. KG).

B. Cells with preset surface alignment

Three types of flat sandwich cells were studied, with the planar, homeotropic, and hybrid anchoring [18] of the local director at the bounding surfaces. Planar cells with indium tin oxide (ITO) electrodes and gap thicknesses $d = (4-23) \mu m$ were either purchased from E.H.C. Co, Japan, or assembled in the laboratory. Planar alignment is achieved by a rubbed layer of polyimide PI2555 (Nissan Chemicals, Ltd.). Homeotropic cells, $d = (2-4) \mu m$, are prepared in the laboratory using the technique developed by Kim [19,20]. The reactive mesogen RM257 is mixed with the homeotropic aligning agent SE5661 and doped with the UV photoinitiator Irgacure 651, in weight proportion SE5661:RM257:Irgacure 651 = 96.7 : 3 :0.3. The mixture is spin coated onto an ITO glass substrate and baked at 170 °C for 1 h. The substrates are then irradiated with UV light (365 nm) for 90 min [19,20]. The cell thickness is set by spherical spacers mixed with UV-curable adhesive NOA68 (Norland Products, Inc.), and the thickness is measured using Lambda 18 UV/VIS spectrometer (Perkin Elmer, Inc). The cells are filled with N and Ch mixtures in the isotropic phase and slowly cooled down (0.2 °C/min) to the desired temperature.

C. Electric field control of the structure

To create the Ch_{OH} state, an alternating current (AC) field with a frequency 3 kHz is applied to the ITO electrodes using Keithley 3390 waveform-function generator (Keithley Instruments) and wideband Krohn-Hite 7602M amplifier

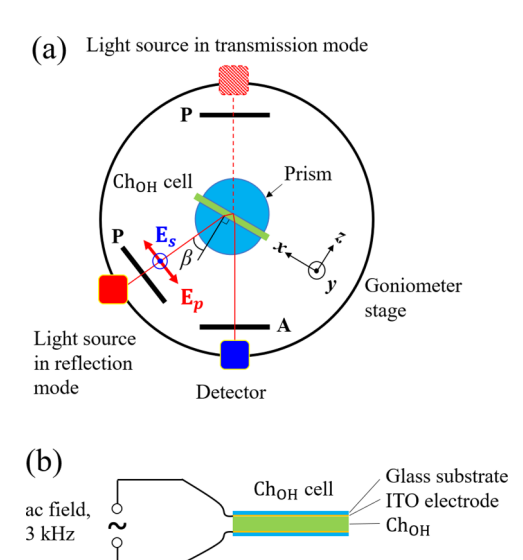


FIG. 2. (a) Reflection and transmission modes of the oblique incidence setup (top view). The xz plane of incidence is parallel to the goniometer stage, and the angle of incidence β is measured from the normal to the Ch_{OH} cell. The polarizations of the incident and reflected rays are set by the polarizer (P) and analyzer (A), respectively. (b) Ch_{OH} cell geometry.

(Krohn-Hite Co.). In the applied field, the helicoidal axis $\hat{\mathbf{h}}$ is parallel to the field \mathbf{E} , $\hat{\mathbf{h}}||\mathbf{E}$, and the Ch_{OH} pitch P is tunable by the field in a broad range [7,8].

The electric field does not cause noticeable heating of cells. A thin homeotropic N cell, $d=4\,\mu\mathrm{m}$, was subject to a 3 kHz AC field, ranging from 1 to 5 V/ $\mu\mathrm{m}$. Phase-transition temperatures measured at different applied voltages showed no changes exceeding 0.1 °C. Other material parameters such as parallel component ε_{\parallel} of dielectric permittivity did not change by more than 2%. This 2% difference is equivalent to a temperature shift by less than 0.05 °C.

D. Spectral measurements: Oblique and normal incidence of light

Optical spectra are measured using a tungsten halogen light source LS-1 with a working range 350–2000 nm and a USB2000 Vis-NIR spectrometer (both Ocean Optics, Inc.). At the normal incidence of light, unpolarized light from the light source is focused by a lens into a paraxial ray. The reflected beam is passed back through the bifurcated fiber and detected by the spectrometer interfaced with the OCEANVIEW spectroscopy software. The Bragg reflection wavelength is measured as a function of the applied electric field, as described previously [6].

In addition to the normal incidence measurements, we use the Bragg reflection for the oblique incidence of light to verify the values of the intrinsic pitch P_0 and the critical electric field E_{NC} (at which the helix is unwound) measured by other techniques (see below). At the oblique incidence of light, Bragg reflection spectra are measured using a fiberoptics setup based on a rotating goniometer stage (Euromex Holland) [Fig. 2(a)]. Polarization of the incident and reflected beams is set by a pair of linear wire-grid polarizers (Thorlabs,

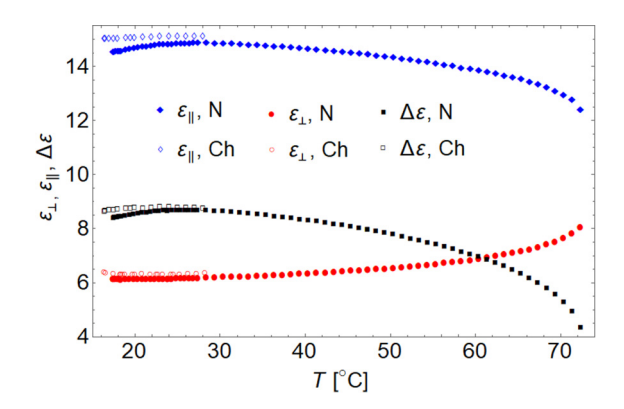


FIG. 3. Temperature dependencies of dielectric permittivities ε_{\parallel} , ε_{\perp} , and $\Delta\varepsilon$ measured in the N and Ch mixtures (filled and empty symbols, respectively).

Inc.) placed along the optical path at the exit from the fiber connected to the light source and at the entrance to the fiber connected to the USB2000 detector. p- and s-polarization states of an electromagnetic wave are defined as the electric field components, \mathbf{E}_p and \mathbf{E}_s , parallel and perpendicular to the plane of incidence, respectively. The Ch_{OH} cell is mounted in the center of the goniometer stage such that the plane of incidence is parallel to the horizontal xz plane. The angle of incidence β , measured from the normal $\hat{\mathbf{z}}$ to the Ch_{OH} cell, is set with an accuracy better than 0.25°. The Ch_{OH} cell is sandwiched between two semicylindrical prisms (N-BK7 glass, $n_p = 1.518$ at 547 nm, DelMar Photonics). A Cargille matching liquid with the refractive index n = 1.516 (at 600 nm) fills the gaps between the cell substrates and prisms to reduce reflection losses. The semicylindrical prisms allow one to measure light reflection in a broad angular range and assure that the angle of incidence from the glass is the same as the incidence angle from the air: $\beta_g = \beta_{air} \equiv \beta$.

Besides the wavelength of Bragg reflection, the determination of K_{22} and K_{33} also requires the knowledge of dielectric anisotropy $\Delta \varepsilon$, ordinary n_o and extraordinary n_e refractive indices, P_0 , and E_{NC} . Below we present the corresponding techniques.

E. Dielectric anisotropy $\Delta \varepsilon$

The dielectric characterization of Ch is performed using an LCR meter 4284A (Hewlett Packard). The parallel permittivity ε_{\parallel} is determined from the capacitance of a homeotropic cell, $d=1.9~\mu\text{m}$, measured at a high electric field $E>E_{NC}$, and the perpendicular permittivity ε_{\perp} is measured in the planar cell, $d=9.1~\mu\text{m}$, by applying a weak electric field $E=10^{-3}~\text{V}/\mu\text{m}$ that does not perturb the planar Ch structure. The dielectric anisotropy $\Delta\varepsilon$ is then calculated as the difference $\varepsilon_{\parallel}-\varepsilon_{\perp}$ (Fig. 3).

F. Birefringence and refractive indices

Birefringence is measured in both the Ch and N mixtures. Ch birefringence is calculated as $\Delta n = \Gamma/d$ [Fig. 4(b)], where Γ is the optical retardance of a thin ($d = 5.3 \,\mu\text{m}$) planar cell with the director unwound by a strong in-plane AC (3 kHz) electric field $E > E_{NC}$, applied to two ITO stripe electrodes

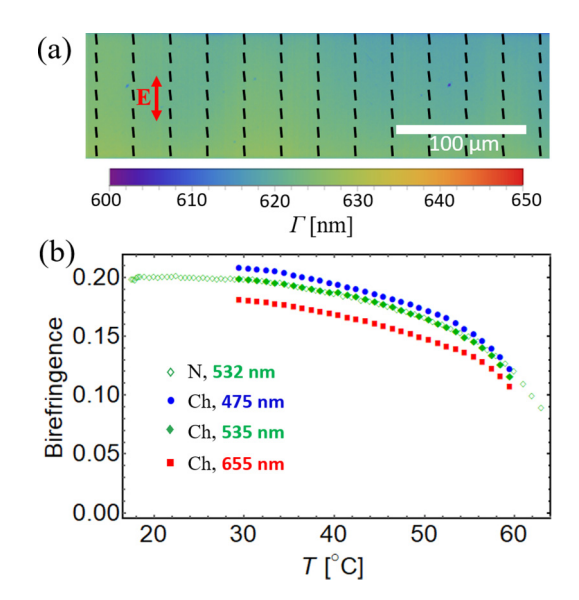


FIG. 4. (a) MicroImager map of the optical retardance of the Ch_{OH} cell subject to a high in-plane electric field $E > E_{NC}$. (b) Temperature dependence of the birefringence measured in N (empty symbols) and Ch (filled symbols) mixtures. The size of all data symbols exceeds the error of measurement.

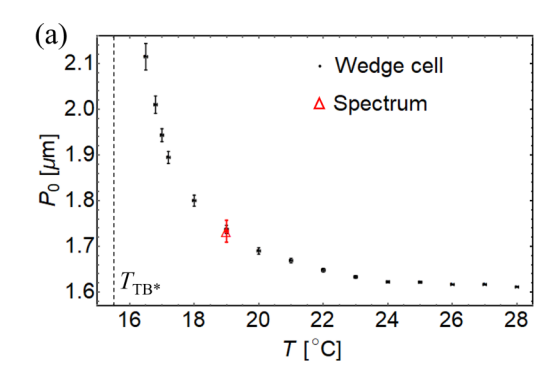
separated by a 100 μ m gap [Fig. 4(a)]. Γ is measured using the Exicor MicroImager System (Hinds Instruments) at three different wavelengths: 475, 535, and 655 nm.

In the N mixture, the ordinary n_o and extraordinary n_e refractive indices are measured using a wedge cell and the interference technique [21]. The wedge cell is assembled from two glass substrates with ITO electrodes coated with rubbed polyimide PI2555 (Nissan Chemicals, Ltd.) to achieve planar alignment. The rubbing direction is perpendicular to the thickness gradient. The thickness of the thick end of the cell is set by 100 μ m spacers mixed with the adhesive NOA68. There are no spacers at the glued wedge. The wedge angle is less than 1° . The cell is filled with the N mixture in the isotropic phase, and the refractive indices are measured at 532 nm on cooling. The Δn values of the Ch and N phases are in very good agreement with each other [Fig. 4(b)]. Therefore, we used the N mixture to determine the dispersion of the ordinary refractive index, which is needed for the extraction of K_{33} from the Bragg spectra.

The dispersion $n_o(\lambda)$ is described by the Cauchy formula $n_o(\lambda) = A + B\lambda^{-2}$. We measure the temperature dependence of n_o at 488, 532, and 633 nm, using laser line color filters with 1 nm central bandwidth (Thorlabs, Inc.). Within the temperature range 3.5 °C $\leq T - T_{\rm TB} \leq$ 6 °C, n_o is practically temperature independent, with the mean values $n_o = 1.564$ at 488 nm, $n_o = 1.560$ at 532 nm, and $n_o = 1.552$ at 633 nm. The polynomial coefficients found by fitting are A = 1.534 and $B = 7.10 \times 10^{-3} \ \mu {\rm m}^2$.

G. Cholesteric pitch P_0

The temperature dependence of the intrinsic Ch pitch P_0 is measured in the absence of the electric field using the Grandjean-Cano wedge cell. The cell is assembled from two ITO glass substrates coated with a rubbed layer of polyimide



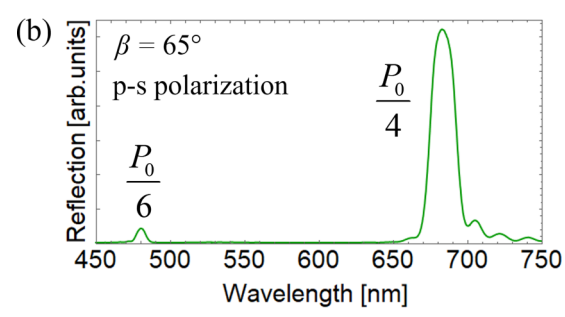


FIG. 5. (a) Temperature dependence of the pitch P_0 (T) measured in the wedge cell and (b) Bragg reflections corresponding to $P_0/4$ and $P_0/6$; oblique incidence of light, Ch_{OH} cell thickness $d=16 \, \mu \text{m}$.

PI2555 to achieve planar alignment. The rubbing direction is perpendicular to the thickness gradient. The thickness of the thick end of the cell is set by 140 μ m glass slides mixed with the adhesive NOA68, and there are no spacers at the glued wedge. The wedge angle is 0.83°. P_0 is determined from the spacing of dislocations of a Burgers vector $P_0/2$ [22]; it increases as the temperature is lowered [Fig. 5(a)].

Since in some cases the Grandjean-Cano wedge approach could produce incorrect results if attention is not being paid to the Burgers vector of the dislocations [22] and to their locations [23,24], we verified the value of P_0 in an independent experiment by measuring the wavelength of Bragg reflection peaks at oblique incidence for a planar Ch cell with $d = 16 \,\mu\text{m}$ at $T = 19 \,^{\circ}\text{C}$ [Fig. 5(b)]. At the fixed angle of incidence $\beta = 65^{\circ}$, we use the p-polarized incident beam and s-polarized reflected beam to obtain the spectrum with two reflection maxima, $\lambda = \bar{n}(\frac{P_0}{m})\cos\beta_{LC}$ that correspond to m = 4 and 6, i.e., to $P_0/4$ and $P_0/6$ values; the angle of light propagation in the liquid crystal β_{LC} is calculated using Snell's law, $\beta_{LC} = \arcsin[(n_g/\bar{n})\sin\beta]$, where \bar{n} is the average of refractive indices, and $n_g = 1.52$ (at 600 nm) is the refractive index of the soda-lime glass. P_0 deduced from the spectra coincides with the data obtained from the Grandjean-Cano wedge [Fig. 5(a)].

H. Critical field E_{NC} of unwinding the Ch_{OH} structure

The critical field E_{NC} , at which the helix is unwound, is determined by measuring the capacitance of thin homeotropic Ch_{OH} cells, d = 1.9, 3.3, and 3.9 μ m while changing the applied electric field [Fig. 6(a)]. At $E = E_{NC}$, the conical angle vanishes and does not change if the field increases further, which results in a clearly visible kink. The change

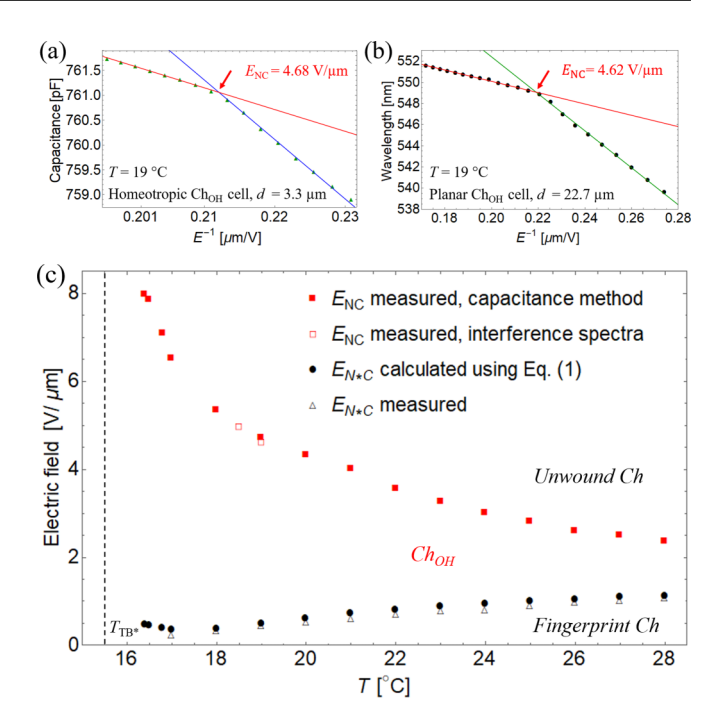


FIG. 6. (a) Capacitance and (b) interference maxima vs electric field; homeotropic Ch_{OH} cell, $d=3.3\,\mu\mathrm{m}$, in the capacitance measurements and the planar Ch_{OH} cell, $d=22.7\,\mu\mathrm{m}$, in the spectral measurements. The kinks correspond to the critical field E_{NC} . (c) Temperature dependence of the critical fields E_{NC} and E_{N*C} ; E_{N*C} is measured experimentally and deduced from Eq. (1).

of capacitance with the field at $E > E_{NC}$ is caused by the suppression of director fluctuations [25].

The critical field E_{NC} was also determined by measuring the transmission spectra through a planar Ch_{OH} cell, d =22.7 μ m, for an oblique incidence, $\beta = 50^{\circ}$. The polarizer P and analyzer A are either parallel or crossed, and both are oriented at 45° with respect to the xz plane of incidence. The field dependency of the light interference extremum shows a similar "kink" at $E = E_{NC}$ [Fig. 6(b)]. Both methods yield very close temperature dependencies of E_{NC} [Fig. 6(c)]. The agreement provides an additional confirmation that the electric field does not cause noticeable heating of cells. Note here that in the studied mixture, the pitch stabilized by the electric fields approaching E_{NC} is very small, decreasing below 50 nm [see Fig. 10(b)]; therefore, the capacitance and interference methods are better suited for the measurements of E_{NC} as compared to Bragg reflection or polarizing microscopy observations of the fingerprint textures [9].

I. Critical field E_{N*C} of the Ch_{OH}-to-Ch transition

Depending on the applied electric field, the Ch cells show three states: an unwound state at $E > E_{NC}$, a Ch_{OH} state at $E_{N*C} < E < E_{NC}$ [Fig. 7(a)], and a Ch state with the director perpendicular to the helicoidal axis, at $E < E_{N*C}$ [9] [Figs. 7(b) and 7(c)]. During the first-order Ch_{OH}-to-Ch structural transition in a hybrid aligned cell, $d = 20.1 \, \mu \text{m}$, caused by the lowering of the electric field, the helical axis $\hat{\mathbf{h}}$ realigns from being parallel to \mathbf{E} in the Ch_{OH} to being perpendicular to it, $\hat{\mathbf{h}} \perp \mathbf{E}$, thus forming a polydomain Ch texture [Fig. 7(c)].

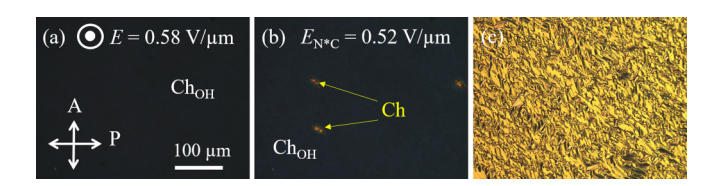


FIG. 7. Polarizing optical microscopy of the Ch_{OH} to Ch transition at T=20 °C: (a) Ch_{OH} texture at $E=0.58\,\mathrm{V/\mu m}$; (b) nucleation of Ch texture, 30 s after the field is reduced to $E_{N*C}=0.52\,\mathrm{V/\mu m}$; (c) expansion of the Ch texture at the same temperature and the applied field, 8 min after the start of nucleation.

The polydomain Ch texture in Fig. 7(c) resembles polydomain textures (often called focal conic domain textures) in Ch cells with homeotropic anchoring at both plates. The similarity is natural since a Ch material with a positive dielectric anisotropy tends to align its helicoidal axis perpendicular to the electric field, in contrast to the ChOH state, in which the helicoidal axis is aligned along the electric field. Furthermore, in the absence of the electric field, the director and thus the Ch helicoidal axis are subject to conflicting homeotropic and planar anchoring conditions at the opposite plates. In the Ch_{OH} state, at $E_{N*C} < E < E_{NC}$, it is the external electric field that aligns the helicoidal axis and stabilizes the heliconical director with twist and bend. The conflicting surface anchoring at the plates results in minor changes of the director field, making the conical angle θ somewhat smaller than its equilibrium bulk value near the homeotropic plate and larger near the planar plate; the thickness of the subsurface layers where θ is different from the bulk value is less than 1 μ m [26]. As demonstrated in the previous study [26], this subsurface change could affect the equilibrium field-stabilized pitch, which could decrease by up to ~ 10 nm in a homeotropic cell and increase by up to ~10 nm in a planar cell. To account for these effects in the measurement of E_{N*C} , we use a hybrid aligned cell, in which the opposite trends mitigate each other, and the overall pitch is close to its equilibrium bulk value expected in infinitely thick samples.

The measured E_{N*C} [Fig. 6(c)] is in good agreement with the theoretical prediction [9],

$$E_{N*C} = E_{NC} \frac{\kappa [2 + \sqrt{2(1 - \kappa)}]}{1 + \kappa},$$
 (1)

based on the comparison of the free energies of the Ch_{OH} and Ch structures; in the evaluation of Eq. (1), we use the elastic ratio $\kappa = K_{33}/K_{22}$ that is presented in the next section.

Both E_{NC} and E_{N*C} define the electric field limits of the Ch_{OH} state. The range of the Ch_{OH} stability widens when one lowers the temperature towards the N_{TB}^* phase.

III. ELASTIC CONSTANTS OF BEND K_{33} AND TWIST K_{22}

The bend constant K_{33} is deduced from the Bragg reflection spectra when unpolarized light is incident normally at a planar Ch_{OH} cell, as described in Ref. [6]. The Bragg wavelength λ_{Bragg} is related to the Ch_{OH} pitch P and K_{33} as [9]

$$\lambda_{\text{Bragg}} = \bar{n}_{\text{eff}} P \text{ and } P = \frac{2\pi}{E} \sqrt{\frac{K_{33}}{\varepsilon_0 \Delta \varepsilon}},$$
 (2)

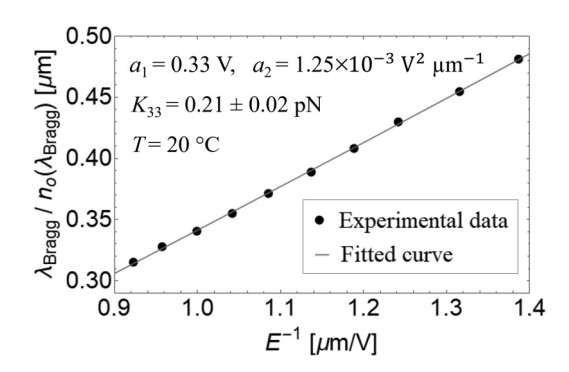


FIG. 8. The field dependence of Bragg reflection wavelength used to calculate K_{33} .

where $\bar{n}_{\rm eff} = (n_o + n_{e, \rm eff})/2$ and $n_{e, \rm eff} = n_o n_e / \sqrt{n_e^2 \cos^2 \theta + n_o^2 \sin^2 \theta}$; for small θ , $n_{e, \rm eff} \approx n_o [1 + \frac{1}{2} (1 - \frac{n_o^2}{n_e^2}) \sin^2 \theta]$. The experimental points $\lambda_{\rm Bragg} / n_o (\lambda_{\rm Bragg})$ are fitted with the polynomial

$$\frac{\lambda_{\text{Bragg}}}{n_o(\lambda_{\text{Bragg}})} = a_1 E^{-1} + a_2 E^{-2} + O(E^{-3}); \tag{3}$$

here, E = U/d, U is the applied voltage, and n_o is interpolated to $\lambda_{\rm Bragg}$ using the experimental data in Fig. 4(b). As demonstrated in Ref. [6], the fitting parameters are such that the a_2 term in Eq. (3) could be neglected, $a_1/a_2E \sim 10^2$, and K_{33} is calculated as

$$K_{33} = \frac{\varepsilon_0 \Delta \varepsilon}{4\pi^2} a_1^2. \tag{4}$$

Figure 8 shows a typical fit of the experimental data with Eq. (3), which confirms that in our experiments, the a_2 term does not affect the deduced K_{33} . Figure 9(a) shows the temperature dependency of K_{33} ; the accuracy of the measured K_{33} is better than 3% in both Figs. 8 and 9(a). To explore whether the boundary conditions could affect the accuracy, the spectra were analyzed also for hybrid cells in the temperature range 16.5-22.0 °C. The two sets of K_{33} data differ by less than 2%.

The twist elastic constant K_{22} is found from the expression [9]

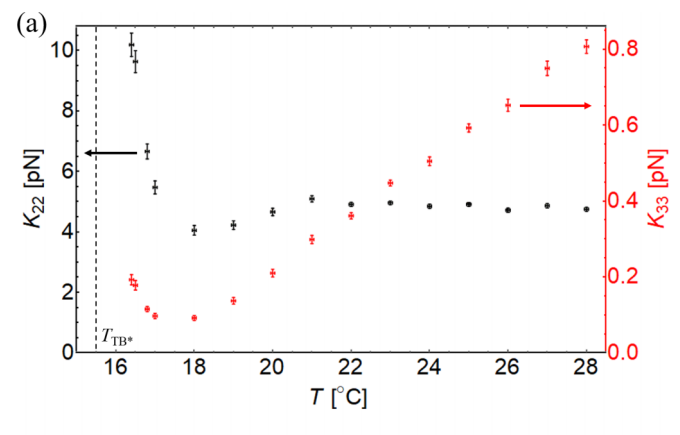
$$K_{22} = \frac{P_0 E_{NC} \sqrt{\varepsilon_0 \Delta \varepsilon K_{33}}}{2\pi}; \tag{5}$$

its temperature dependence is shown in Fig. 9(a). Since both the intrinsic pitch P_0 and K_{22} are known, we could deduce the temperature dependence of the chiral parameter $K_C = 2\pi K_{22}/P_0$, which could also be expressed as $K_C = E_{NC}\sqrt{\varepsilon_0\Delta\varepsilon K_{33}}$ using Eq. (5); see Fig. 9(b).

The Ch_{OH} structure depends critically on K_{22} and K_{33} . The effect is understandable since Ch_{OH} could exist only if K_{33} is sufficiently small to allow the heliconical structure with both twist and bend. The elastic anisotropy ratio $\kappa = K_{33}/K_{22}$ determines the range of the electric field tunability of the Ch_{OH} pitch P and the conical angle θ [9],

$$P = \frac{\kappa E_{NC} P_0}{F},\tag{6}$$

$$\sin^2\theta = \frac{\kappa}{1-\kappa} \Big(\frac{E_{NC}}{E} - 1 \Big). \tag{7}$$



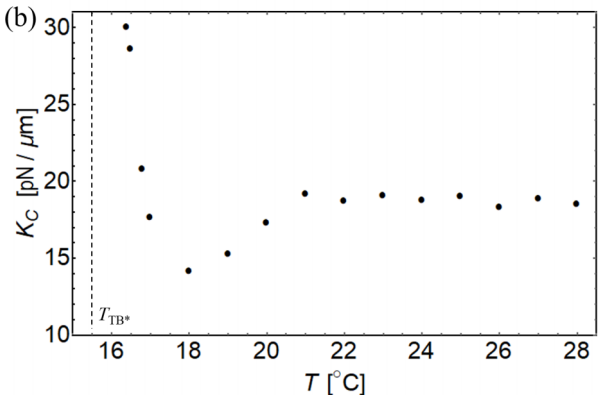


FIG. 9. (a) Temperature dependencies of K_{33} and K_{22} , and (b) chiral parameter K_C .

The elastic ratios κ and $\kappa/(1-\kappa)$ in Eqs. (6) and (7) show a strong temperature dependency [Fig. 10(a)], which implies that the optical properties such as the Bragg reflection wavelength (related to P) and the width of the Bragg peak (related to θ) are also temperature dependent. Substituting $E = E_{N*C}$ and $E = E_{NC}$ into Eq. (6), one can determine the largest $P_{N*C} = \frac{(1+\kappa)P_0}{2+\sqrt{2-2\kappa}}$ and the smallest $P_{NC} = \kappa P_0$ pitch [Fig. 10(b)]. The tunable Ch_{OH} pitch range $P_{NC} < P < P_{N*C}$

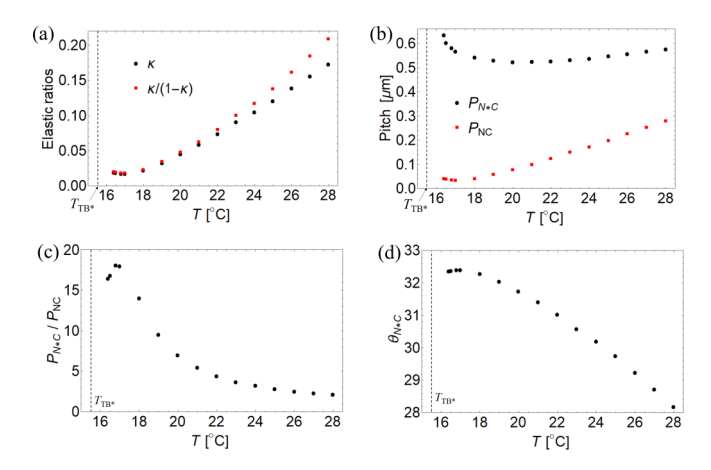


FIG.10. Temperature dependencies of (a) the elastic ratios κ and $\kappa/(1-\kappa)$, (b) maximum P_{N*C} and minimum P_{NC} Ch_{OH} pitches, (c) ratio of the pitches P_{N*C}/P_{NC} , and (d) maximum opening cone angle θ_{N*C} .

is very broad near the $Ch-N_{TB}^*$ transition temperature, where the ratio P_{N*C}/P_{NC} is about 18 [Fig. 10(c)], which means that the electric field could tune the wavelength of Bragg reflection in an extraordinary broad range. Broadening of the Ch_{OH} pitch range is caused by a steep decrease of K_{33} near the $Ch-N_{TB}^*$ phase transition. Finally, the smallest field at which the Ch_{OH} state still exists, $E=E_{N*C}$ in Eq. (7), defines the widest cone angle of the heliconical structure θ_{N*C} , which reaches about 32.4° near the transition to the N_{TB}^* phase [Fig. 10(d)]. Since our experiments confirm the validity of Eq. (1) for E_{N*C} [see Fig. 6(c)], we could use Eq. (1) and Eq. (6) to demonstrate that θ_{N*C} is fully determined by the elastic ratio κ :

$$\cos^2 \theta_{N*C} = \frac{1}{\sqrt{2(1-\kappa)}}.$$
 (8)

In the limit $\kappa = 0$, the widest possible θ_{N*C} is 32.8°; if $\kappa > 1/2$, the Ch_{OH} state does not occur.

IV. CONCLUSIONS

We measured the elastic constants of twist K_{22} and bend K_{33} directly in a chiral nematic, using electrically tunable Bragg reflection of light from the Ch_{OH} state and the critical field of unwinding the ChOH structure, as well as the material properties such as dielectric anisotropy, off-field cholesteric pitch, and refractive indices. The measurements were made possible by introducing two independent techniques, based on capacitance and interference measurements, to determine the critical field E_{NC} , at which the Ch_{OH} state unwinds into a uniform structure. The corresponding pitch at the fields approaching E_{NC} is so small (decreasing below 50 nm) that seemingly straightforward approaches such as Bragg reflection in the visible part of the spectrum, or microscopy observations of textures, are not applicable. The proposed approach allowed us to demonstrate a very broad range of pitch tunability. For the studied mixture, we find that the ratio of the largest to smallest pitch in the electrically tunable range is about 18; a similar ratio is expected for the tunable Bragg reflection of light.

The ratio of elastic constants $\kappa = K_{33}/K_{22}$ is small, in the range 0.017–0.2 in a wide temperature range (>10 °C) above the transition to the chiral twist-bend nematic phase. The smallness of κ explains the broad temperature range of the existence of the Ch_{OH} structure that allows one to continuously tune the wavelength of Bragg reflection by an external field. The temperature dependencies $K_{22}(T)$ and $K_{33}(T)$ allow us to characterize the ChOH structure, namely, determine the range of the electrically tunable pitch P and the maximum cone angle θ . These dependencies are of interest on their own, as both K_{22} and especially K_{33} increase rapidly near the $Ch - N_{TB}^*$ transition [Fig. 9(a)]. Similar behavior is known in nematics [17,23,27,28] and cholesterics [6,24] that show a transition to N_{TB} or N_{TB}^* . The increase of K_{22} and K_{33} is also well established in materials in which the nematic [29] or cholesteric [5] phase experiences a transition into a smectic A phase. Similar to the case of smectics, the nuclei of the $N_{\rm TB}$ or $N_{\rm TB}^*$ phases make the bend and twist of the director difficult because these deformations are incompatible with the equidistance of the pseudolayered structure. Interestingly, K_{22} shows a nonmonotonous temperature dependence, with a minimum that precedes a rapid increase upon cooling [Fig. 9(a)]. Although unusual, this behavior is similar to the one observed for K_{22} in the nematic phase of pure CB7CB when the temperature approaches the $N_{\rm TB}$ phase [17]. Furthermore, the temperature dependence of the ratio K_{33}/K_{22} in Fig. 10(a) and in pure CB7CB [17] are qualitatively the same, showing that K_{33} diverges more rapidly than K_{22} near the transition to $N_{\rm TB}$.

The intrinsic (field-free) pitch P_0 of the Ch increases as the temperature is lowered (Fig. 5). Similar behavior of the Ch pitch is observed near the transition to the smectic A [5] and N_{TB}^* phase [24,30]. The trend could be again explained by the proximity to pseudolayered N_{TB} and N_{TB}^* phases, but Oswald and Dequidt [24] proposed an additional mechanism, rooted in the possibility that N_{TB}^* nuclei impose an opposite sense of

chirality onto the surrounding Ch background [24]. Similar to K_{22} , the linear chiral term $K_C = 2\pi K_{22}/P_0$ in the elastic energy density of Ch shows a nonmonotonic temperature behavior: K_C is nearly constant far away from N_{TB}^* , then shows a minimum and a rapid increase as the temperature is lowered towards N_{TB}^* [Fig. 9(b)]. The decrease might be qualitatively explained by the Oswald-Dequidt model [24], in which the Ch helicoid is partially unwound by N_{TB}^* nuclei (which implies an increase of P_0), followed by the strong increase of K_{22} .

ACKNOWLEDGMENT

The work was supported by the NSF Grant No. ECCS-1906104.

- [1] P. G. de Gennes and J. Prost, *The Physics of Liquid Crystals* (Clarendon Press, Oxford, 1995).
- [2] M. Kleman and O. D. Lavrentovich, *Soft Matter Physics: An Introduction* (Springer-Verlag, New York, 2003).
- [3] L. M. Blinov, Electrooptic Effects in Liquid Crystal Materials (Springer-Verlag, New York, 1994).
- [4] W. H. de Jeu, *Physical Properties of Liquid Crystalline Materials* (CRC Press, Boca Raton, FL, 1980), Vol. 1.
- [5] F. Zhang and D. K. Yang, Liq. Cryst. 29, 1497 (2002).
- [6] O. S. Iadlovska et al., Phys. Rev. Research 2, 013248 (2020).
- [7] R. B. Meyer, Appl. Phys. Lett. 12, 281 (1968).
- [8] P. G. de Gennes, Solid State Commun. 6, 163 (1968).
- [9] J. Xiang, S. V. Shiyanovskii, C. Imrie, and O. D. Lavrentovich, Phys. Rev. Lett. 112, 217801 (2014).
- [10] J. Xiang, Y. Li, Q. Li, D. A. Paterson, J. M. D. Storey, C. T. Imrie, and O. D. Lavrentovich, Adv. Mater. 27, 3014 (2015).
- [11] S. M. Salili et al., Phys. Rev. E 94, 042705 (2016).
- [12] G. Nava, F. Ciciulla, O. S. Iadlovska, O. D. Lavrentovich, F. Simoni, and L. Lucchetti, Phys. Rev. Research 1, 033215 (2019).
- [13] V. Borshch et al., Nat. Commun. 4, 2635 (2013).
- [14] D. Chen et al., Proc. Natl. Acad. Sci. 110, 15931 (2013).
- [15] D. A. Paterson, M. Gao, Y.-K. Kim, A. Jamali, K. L. Finley, B. Robles-Hernández, S. Diez-Berart, J. Salud, M. R. de la Fuente, B. A. Timimi *et al.*, Soft Matter 12, 6827 (2016).
- [16] G. Cukrov, Y. Mosaddeghian Golestani, J. Xiang, Yu. A. Nastishin, Z. Ahmed, C. Welch, G. H. Mehl, and O. D. Lavrentovich, Liq. Cryst. 44, 219 (2017).
- [17] G. Babakhanova, Z. Parsouzi, S. Paladugu, H. Wang, Yu. A. Nastishin, S. V. Shiyanovskii, S. Sprunt, and O. D. Lavrentovich, Phys. Rev. E 96, 062704 (2017).

- [18] K. Thapa, O. S. Iadlovska, H. K. Bisoyi, D. A. Paterson, J. M. D. Storey, C. T. Imrie, Q. Li, S. V. Shiyanovskii, and O. D. Lavrentovich, Phys. Rev. E 104, 044702 (2021).
- [19] Y.-K. Kim, G. Cukrov, F. Vita, E. Scharrer, E. T. Samulski, O. Francescangeli, and O. D. Lavrentovich, Phys. Rev. E 93, 062701 (2016).
- [20] G. Babakhanova and O. D. Lavrentovich, in *Modern Problems of the Physics of Liquid Systems*, edited by L. A. Bulavin and L. Xu, Springer Proceedings in Physics, Vol 223 (Springer International Publishing, Cham, 2019), pp. 165–197, doi: 10. 1007/978-3-030-21755-6_7.
- [21] J. Kędzierski et al., OptoElectron. Rev. 18, 214 (2010).
- [22] I. I. Smalyukh and O. D. Lavrentovich, Phys. Rev. E **66**, 051703 (2002).
- [23] P. Oswald and J. Colombier, Liq. Cryst. 48, 1608 (2021).
- [24] P. Oswald and A. Dequidt, Phys. Rev. E 105, 024707 (2022).
- [25] V. Borshch, S. V. Shiyanovskii, B.-X. Li, and O. D. Lavrentovich, Phys. Rev. E **90**, 062504 (2014).
- [26] O. S. Iadlovska, G. R. Maxwell, G. Babakhanova, G. H. Mehl, C. Welch, S. V. Shiyanovskii, and O. D. Lavrentovich, Opt. Lett. 43, 1850 (2018).
- [27] A. Aouini, M. Nobili, E. Chauveau, P. Dieudonné-George, G. Damême, D. Stoenescu, I. Dozov, and C. Blanc, Crystals 10, 1110 (2020).
- [28] G. Babakhanova, H. Wang, M. Rajabi, D. Li, Q. Li, and O. D. Lavrentovich, Liq. Cryst. 1 (2022).
- [29] P. P. Karat and N. V. Madhusudana, Mol. Cryst. Liq. Cryst. 40, 239 (1977).
- [30] N. A. Kasian, L. N. Lisetski, and I. A. Gvozdovskyy, Liq. Cryst. 49, 142 (2022).